The First Habitable Zone Earth-sized Planet from TESS. III: Climate States and Characterization Prospects for TOI-700 d

Gabrielle Suissa,[1,2,3] Eric T. Wolf,[2,4,5] Ravi kumar Kopparapu,[1,2,5] Geronimo L. Villanueva,[1,2] Thomas Fauchez,[1,2,3] Avi M. Mandell,[1,2] Giada Arney,[1,2,5] Emily A. Gilbert,[1,2,6,7] Joshua E. Schlieder,[1,2] Thomas Barclay,[1,2,8] Elisa V. Quintana,[1,2] Eric Lopez,[1,2] Joseph E. Rodriguez,[9] and Andrew Vanderburg[10,11]

[1] NASA Goddard Space Flight Center, 8800 Greenbelt Rd, Greenbelt, MD 20771, USA
[2] NASA Goddard Sellers Exoplanet Environments Collaboration
[3] Goddard Earth Sciences Technology and Research (GESTAR), Universities Space Research Association, Columbia, Maryland, USA
[4] Laboratory for Atmospheric and Space Physics, Department of Atmospheric and Oceanic Sciences, University of Colorado Boulder, Boulder, CO 80309, USA
[5] NASA NExSS Virtual Planetary Laboratory, Box 951580, Seattle, WA 98195
[6] Department of Astronomy and Astrophysics, University of Chicago, 5640 S. Ellis Ave, Chicago, IL 60637, USA
[7] The Adler Planetarium, 1300 South Lakeshore Drive, Chicago, IL 60605, USA
[8] University of Maryland, Baltimore County, 1000 Hilltop Cir, Baltimore, MD 21250, USA
[9] Center for Astrophysics | Harvard & Smithsonian, 60 Garden St, Cambridge, MA, 02138, USA
[10] Department of Astronomy, The University of Texas at Austin, Austin, TX 78712, USA
[11] NASA Sagan Fellow

(Dated: December 2019)

ABSTRACT

We present self-consistent three-dimensional climate simulations of possible habitable states for the newly discovered Habitable Zone Earth-sized planet, TOI-700 d. We explore a variety of atmospheric compositions, pressures, and rotation states for both ocean-covered and completely desiccated planets in order to assess the planet's potential for habitability. For all 20 of our simulated cases, we use our climate model outputs to synthesize transmission spectra, combined-light spectra, and integrated broadband phase curves. These climatologically-informed observables will help the community assess the technological capabilities necessary for future characterization of this planet, as well as distinguish possible climate states if one day we do obtain sensitive spectral observations. We find that TOI-700 d is a robust candidate for a habitable world and can potentially maintain temperate surface conditions under a wide variety of atmospheric compositions. Unfortunately, the spectral feature depths from the resulting transmission spectra and the peak flux and variations from our synthesized phase curves do not exceed 10 ppm. This will likely prohibit the James Webb Space Telescope (JWST) from characterizing its atmosphere; however, this motivates the community to invest in future instrumentation that perhaps can one day reveal the true nature of TOI-700 d.

Keywords: planets and satellites: atmospheres – planets and satellites: detection – planets and satellites: terrestrial planets – stars: low-mass

1. INTRODUCTION

The Transiting Exoplanet Survey Satellite (TESS, Ricker et al. 2015) is ushering the field of exoplanets into a new era with its objective to detect small planets around bright stars in the solar neighborhood. Terrestrial-sized planets discovered by TESS pose an exciting opportunity for the community to perform follow up observations with the James Webb Space Telescope (JWST), ground-based observatories, and future flagship missions to characterize their atmospheres. In particular,

Corresponding author: Gabrielle Suissa
gabrielle.engelmann-suissa@nasa.gov

rocky planets in the Habitable Zone (HZ) of cool stars (M dwarfs) are our most promising targets to search for biosignatures in the near future, because they are in the region around a star where liquid water could exist on the surface of a planet, and the relatively large planet-to-star size ratio and frequent transits makes planets orbiting M-dwarf stars more amenable for observations. The TOI-700 system is a newly discovered TESS system of three planets around an M star with an effective temperature of 3480 K. TOI-700 d, the third planet from the star, has an orbital period of 37 days and receives an incident flux of 0.86 S$_\odot$ (Gilbert et al. submitted, Rodriguez et al. submitted), which puts it in the conservative HZ (Kopparapu et al. 2017). It has a derived radius of ∼1.2 R$_\oplus$ and an estimated mass of ∼1.7 M$_\oplus$ (Gilbert et al. submitted, Rodriguez et al. submitted). Observations of other, hotter planets suggest that TOI-700 d is rocky, though there are significant uncertainties in extrapolating these observations to colder, habitable-zone planets like TOI-700 d (Rogers 2015).

As TOI-700 d is in the HZ of an M star, we expect the planet to be tidally locked, and because its eccentricity is close to zero, it is possible that it is in synchronous rotation such that one side of the planet always faces the star (Dobrovolskis 2009; Barnes et al. 2013; Barnes 2017; Leconte et al. 2015). This slow and synchronous rotation leads to complicated and unique atmospheric circulation patterns – the Coriolis effect dictating the circulation weakens, clouds congregate around the substellar point, and heat is transported radially from the dayside of the planet (Yang et al. 2013, 2014; Kopparapu et al. 2016; Way et al. 2016; Haqq-Misra et al. 2018; Wolf et al. 2019; Komacek & Abbot 2019; Del Genio et al. 2019). These inherently three-dimensional effects can only be captured through the usage of three-dimensional general circulation models (GCMs). In this work, we perform GCM simulations to model different planetary atmospheres suitable for TOI-700 d given its parameters. We explore a grid of potentially habitable climate states, with different axes of comparisons such as varying atmospheric compositions, atmospheric pressures, surface conditions, and orbital phenomena. For each simulation, we produce its corresponding synthesized transmission spectra, combined-light (thermal emission and reflected light) phase-dependent spectra, and integrated broadband phase curve. The modeled climates and associated observables will inform the community on how to interpret future spectral retrievals of TOI-700 d, and what technological sensitivity is required to do so.

The history of the field of exoplanets tells us to expect the unexpected, and this very may well hold true upon future characterizations of TOI-700 d. We recognize that our grid of simulations does not represent an exhaustive treatment of all potential realities for TOI-700 d. Due to the limitations of our current 3-D model design, we do not consider O$_2$ dominated post-runaway atmospheres (e.g., Luger & Barnes 2015), nor thick ∼100 bar (and higher) modern Venus-like (e.g., Kane et al. 2014) or sub-Neptunian atmospheres (e.g., Lopez & Fortney 2014). We do not treat prognostic photochemistry in our code nor haze formation, precluding us from considering Titan-analog worlds, complex oxygen dominated chemistry, or other photochemical effects. It is also possible that TOI-700 d has suffered from intense atmospheric escape during the pre-main sequence phase of the star and lacks an atmosphere entirely – although we note that presently TOI-700 has no indications of significant stellar activity, deeming it a quiet star. Here, our focus is simply on potentially habitable climates for TOI-700 d. We limit our study to a set of 20 common habitable atmospheric assumptions that have been widely used by the exoplanet climate modeling community in previous 3-D modeling studies of habitable zone boundaries and of other target objects. In this work, we take a first cut at 3-D modeling potential climates of TOI-700 d, evaluating its potential for habitability, and assessing the requirements for future observation and characterization.

While no model is without limitations, there are several distinct advantages for using a 3-D climate model to inform our synthetic observables. First, it is well known that clouds pose a significant challenge for characterizing the atmospheres of terrestrial class extrasolar planets (Kreidberg et al. 2014; Lincowski et al. 2018; Fauchez et al. 2019; Suissa et al. 2019). 3-D climate models allow for the self-consistent and prognostic calculation of cloud fields, based on the confluence of temperature, moisture, and atmospheric circulations. The search for habitable worlds is the search for water. However, given typical lapse rates in planetary atmospheres, any planet with abundant surface liquid water will have water clouds. Accurately accounting for clouds in our models is critical for interpreting observations. Furthermore, 3-D climate models allow for the self-consistent calculation of horizontal heat transport, which is important on tidally locked planets, and critical for determining phase-dependent observations. The inclusion of prognostic clouds and horizontal heat transport are necessary for determining day-to-night differences in the thermal energy emitted from these worlds, and for calculating full thermal emission phase curves (Yang et al. 2014; Koll & Abbot 2015; Wolf et al. 2019).

This paper is outlined as follows. In Section 2, we detail the suite of GCM simulations we ran and the radiative transfer tools we used. In Section 3 we present transmission spectra and combined phase curves for a selection of our models. In Section 4 we discuss the implications of the observability of the atmosphere of TOI-700 d. For more details about the discovery of the

TOI-700 system and the Spitzer confirmation of TOI-700 d, please see our companion papers I & II: Gilbert et al. (submitted) & Rodriguez et al. 2020 (submitted).

2. METHODS

2.1. *Overview of Climate Models*

In this work we use a three-dimensional general circulation and climate system model to simulate self-consistent atmospheres for the newly discovered planet TOI-700 d. We use the ExoCAM[1,2] modeling package, which is a modified version of the Community Atmosphere Model (CAM) version 4 from the National Center for Atmospheric Research in Boulder, CO (Neale et al. 2010). ExoCAM includes model configurations, source code modifications, and initial conditions files needed to facilitate exoplanet studies. It has been used in numerous climate studies of terrestrial extrasolar planets (Kopparapu et al. 2017; Wolf 2017; Wolf et al. 2019; Haqq-Misra et al. 2018; Komacek et al. 2019b; Komacek & Abbot 2019; Adams et al. 2019; Yang et al. 2019a; Kang 2019). Here, we use ExoCAM to conduct simulations of TOI-700 d considering a variety of atmospheric compositions and planet archetypes that are typically associated with habitable worlds. We consider both aquaplanets (completely ocean-covered with no land) and land-covered planets (completely land-covered with no ocean), with atmospheres composed of varying mixtures of N_2, CO_2, CH_4, H_2, and H_2O.

For aquaplanet simulations, we assume a 50 meter deep slab ocean with no ocean heat transport (OHT). Note that OHT can modulate surface temperatures (Del Genio et al. 2019; Yang et al. 2019b), particularly for cooler planets that lack emergent continents. However, we do not expect OHT to significantly affect the resulting transmission spectra. While OHT may indeed bring more clouds toward the terminator region, a significant change in their average altitude is not expected. Yet it is the altitude of the cloud deck that impacts the transmission spectra the most; it has been shown (Fauchez et al. 2019) that even a small cloud coverage (20% or less) is enough to raise the continuum level above the cloud deck. OHT could also affect thermal emission phase curve morphologies (e.g., Yang et al. 2019b). However, Fujii et al. (2017) found that stratospheric water vapor on tidally locked planets is not strongly affected by OHT, while Yang et al. (2019b) determine that the role of OHT diminishes on warm ($T_S > 290$ K) tidally locked worlds. The presence and location of any emergent continents remains a significant uncertainty for any dynamic ocean model calculations, as continents dramatically change or even halt day-to-night side OHT on tidally locked planets, depending upon the specific continental configuration that is assumed (Del Genio et al. 2019; Yang et al. 2019b). For aquaplanet simulations, we assume that sea ice forms whenever sea surface temperatures fall below the freezing point of seawater at 271.36 K. We also assume the default snow and ice albedo parameterizations, which divide ocean, sea ice, and snow albedos into two bands: visible and near-IR divided at ~0.7 μm. Following Shields et al. (2013), we set the visible (near-IR) sea ice albedo to 0.67 (0.3), the snow albedo to 0.8 (0.68), and the ocean albedo to 0.07 (0.06). For land planet simulations we assume a completely desiccated planet, with a uniform surface composed of sand with an albedo of 0.3 at all wavelengths.

The ExoCAM radiative transfer module, originally constructed for early Earth studies (Wolf & Toon 2013), uses 28 spectral intervals across all wavelengths, with HITRAN 2004 absorption coefficients for H_2O, CO_2, and CH_4. Water vapor continua are included using the MT_CKD model (Clough et al. 2005). CO_2 self-broadening is taken to be 1.3 times the foreign-broadening component while H_2O foreign broadening is assumed to be that of Earth-air. We follow the "MTCKD" parameterization described in Halevy et al. (2009), and at high-CO_2 our method produces intermediate-strength absorption compared to other popular CO_2 continuum parameterizations (Halevy et al. 2009). Collision induced absorption are included for N_2-N_2, H_2-H_2, and N_2-H_2 pairs. Note that while this particular set of absorption coefficients is older and biases towards overestimating near-IR absorption in water-rich atmospheres (Yang et al. 2016), model comparisons of full 3-D climate simulations against other models with updated absorption coefficients are in reasonable agreement for planets around M-dwarf stars (Wolf 2018; Fauchez et al. 2019).

Simulations were run with 4°×5° horizontal resolution and 51 vertical layers extending from the surface up to ~0.01 mbar pressures, using a finite-volume dynamical core (Lin & Rood 1996). The high model top allows for a better representation of upper level water vapor and clouds, which is critical for calculating synthetic transmission spectra (Suissa et al. 2019). All simulations are initiated from present-day Earth global mean surface temperatures, and run until the top-of-atmosphere

---

[1] https://github.com/storyofthewolf/ExoCAM
[2] https://github.com/storyofthewolf/ExoRT

Star	
Mass ($M_\odot$)	0.4151
Radius ($R_\odot$)	0.4185
Luminosity ($L_\odot$)	0.0232
Log g	4.81
Metallicity	0
Planet	
Period (days)	37.43
Mass ($M_\oplus$)	1.423
Radius ($R_\oplus$)	1.115
Surface gravity (m/s^2)	11.24
Semi major axis (AU)	0.163356
Stellar flux (W/m^2)	1183.36

Table 1. Parameters for TOI-700 and TOI-700 d used in this work's simulations. These parameters vary compared to those presented in the final version of Gilbert et al. (submitted), yet they remain within 1σ of the published values.

energy balance reaches equilibrium, taking 30 to 100 years depending on the specific simulation. Note that recent works indicate that Snowball hysteresis does not occur for tidally locked planets around M dwarfs (Checlair et al. 2017, 2019); thus we expect our results to be unchanged for different assumptions of the initial temperature fields. The atmospheric constituents N_2, CO_2, CH_4, and H_2 are assumed to be well mixed in the atmosphere. However, H_2O and water clouds vary self-consistently with the ambient meteorological conditions calculated in the model. Liquid cloud particle sizes are set to a constant value of 14 μm, while ice cloud particle sizes rely on a temperature-dependent function and can range in size from up to several hundred μm.

Table 1 lists the stellar and planetary system properties used in our 3-D simulations. These parameters vary slightly compared to those presented in the final version of the discovery paper, Gilbert et al. (submitted), as they have continued to refine their estimates. Still, our values remain within 1σ of the final numbers. We note that the additional data and independent analysis performed by Rodriguez et al. (submitted) suggests a slightly larger radius for TOI-700 d. Though their radius is slightly more than 1σ above the value we use in our simulations, we do not expect a larger radius of 1.2 $R_\oplus$ and a consequently larger mass to significantly impact our results. For the input stellar spectra we interpolate from the BT-Settl spectral models (Allard et al. 2007) to construct a TOI-700 specific spectrum, with T_{eff} = 3480 K, [Fe/H] = 0, and log g = 4.81. We assume that TOI-700 d is synchronously rotating, meaning the planetary rotation period equals its orbital period (37.43 Earth days), for all cases except where specifically noted. We also run two simulations where we assume that the planet is in a 2:1 spin-orbit resonance, meaning that the planet experiences one diurnal period per orbit.

Our simulation grid is summarized in Table 2. We consider three different archetypes of atmospheric compositions. "Modern Earth" in this work refers to an atmosphere with a N_2 dominated pressure of 1 bar, 400 ppm CO_2, 1.7 ppm CH_4. O_2 is not considered in this study because it does not significantly affect planetary climate, acting primarily as background gas contributing to pressure broadening and molecular scattering effects. "Archean Earth" in this work is inspired by our understanding of our planet's early history, where higher levels of CO_2 and CH_4 than we experience today were required to keep the planet warm despite the faint young Sun. "Early Mars" is loosely used to describe a CO_2 dominated atmosphere, which would have been required for liquid water to exist on early Mars. The three above archetypes are explored both as completely ocean-covered aquaplanets and as completely desiccated land-covered planets. We also include a "plain" aquaplanet case, with only H_2O and N_2 and an atmospheric pressure of 1 bar, and an "H_2-supporting" case with atmospheric abundances similar to that of an "Archean Earth" except with 0.1 bar of H_2, inspired by solutions for the faint young Sun paradox posed by Wordsworth & Pierrehumbert (2013). In addition, we examine the "Archean Earth" and "Early Mars" archetypes with different atmospheric pressures for both desiccated and aquaplanet planets, ranging from 0.5 bar to 10 bar in some cases. Finally, we analyze the effect of orbital phenomenon for one of the aqua and land "Archean Earth" cases, by experimenting with a 2:1 rotation:orbital resonance instead of synchronous rotation.

	Aqua		Desiccated	
	Atmospheric Specifications	*Atm. Pressure*	*Atmospheric Specifications*	*Atm. Pressure*
"Modern Earth"	400 ppm CO_2, 1.7 ppm CH_4	1 bar	400 ppm CO_2, 1.7 ppm CH_4	1 bar
"Archean Earth"	0.01 bar CO_2, 0.0001 bar CH_4	1 bar	0.1 bar CO_2, 0.001 bar CH_4	1 bar — Synch. / 2:1
	0.1 bar CO_2, 0.001 bar CH_4	0.5 bar; 1 bar (Synch.; 2:1); 4 bar; 10 bar		
	0.1 bar CO_2, 0.002 bar CH_4	1 bar		
"Early Mars"	CO_2 dominated	0.5 bar; 1 bar; 2 bar; 4 bar	CO_2 dominated	1 bar; 4 bar; 10 bar
"H_2-supporting"	N_2 dominated 0.1 bar CO_2, 0.001 bar CH_4, 0.1 bar H_2	1 bar		
"Plain"	N_2 dominated	1 bar		

Table 2. Grid of simulations used in this work. We explored different compositions, surface types (aquaplanet vs desiccated), atmospheric pressures, and orbital phenomenon (synchronously rotating or in a 2:1 rotation:orbital resonance).

Our GCM simulations include N_2 and Earth's most significant greenhouse gases: CO_2, CH_4 and H_2O. We do not include other gases such as O_2, O_3, or C_2H_6 because these gases are not expected to impact the climate as strongly and/or because their abundances are challenging to predict in a self-consistent way without a photochemical model. We anticipate that including photochemistry would affect the abundances and vertical profiles of gases in our atmospheres, and this is an important avenue of future work. For example, Segura et al. (2005) show that a modern-Earth-like planet orbiting an M dwarf can result in the planet's atmosphere accumulating over two orders of magnitude more CH_4 compared to the same planet around the Sun. This is because M dwarfs produce less radiation near 300 nm where O_3 is photolyzed. Oxygen radicals generated by this photolysis are the dominant sink of CH_4 in modern Earth's atmosphere; with the decrease of this photolysis rate comes the potential increase in CH_4 abundance for planets around M dwarfs. Additionally, organic haze formation can initiate if the CH_4/CO_2 ratio exceeds 0.1 (Trainer et al. 2004; Arney et al. 2016, 2017); however in our simulated atmospheres, methane abundances are kept below this level, and thus photochemical hazes would not be expected to form.

2.2. *The Planetary Spectrum Generator and GlobES*

We synthesize transmission and emission spectra with the Planetary Spectrum Generator (PSG, https://psg.gsfc.nasa.gov/, Villanueva et al. 2018). PSG is a spectroscopic suite that integrates the latest radiative transfer methods and spectroscopic parameterizations, and includes a realistic treatment of multiple scattering in layer-by-layer spherical geometry. Specifically, multiple scattering from atmospheric aerosols is enabled within PSG using the discrete ordinates method, in which the radiation field is approximated by a discrete number of streams distributed in angle with respect to the plane-parallel normal. The angular dependence of the scattering phase function for a particular aerosol is described in terms of an expansion in terms of Legendre Polynomials, typically with the number of expansion terms equal to the number of stream pairs. As implemented in PSG, the Legendre expansion coefficients are pre-computed using an assumed particle size distribution for each available aerosol type (e.g., Massie & Hervig 2013). PSG permits the ingestion of billions of spectral lines of over 1,000 species from several spectroscopic repositories (e.g., HITRAN, JPL, CDMS, GSFC-Fluor). For this investigation, the molecular spectroscopy is based on the latest HITRAN database (Gordon et al. 2017), which is complemented by UV/optical data from the MPI database (Keller-Rudek et al. 2013).

In order to capture the heterogeneous properties of the atmosphere and the surface as determined by the GCM, the GlobES (Global Exoplanetary Spectra, https://psg.gsfc.nasa.gov/apps/globes.php) module of PSG was used to compute combined emission and reflection spectra across the observable disk. PSG currently provides templates and conversion scripts for several GCM models, including ROCKE-3D (Way et al. 2017), Laboratoire de Météorologie Dynamique (LMD, Forget et al. 1999; Hourdin et al. 2006; Wordsworth et al. 2011), and the Community Atmosphere Model (CAM, Neale et al. 2010) as used for this investigation. We ingested the ExoCAM GCM-generated vertical profiles of temperature, pressure, volume mixing ratios of molecular species, and mass mixing ratios and particles sizes for liquid and water ice clouds into GlobES at every 4° of latitude across the terminator to create a local spectrum. We then averaged all of the resulting local spectra to create an average terminator spectrum for the planet. For direct imaging and secondary eclipse simulations, GlobES performs radiative transfer simulations across the whole observable disk considering the appropriate incidence, emission, and phase angles for that grid point, while the individual spectra are integrated considering the projected area of each bin.

When creating combined emitted and reflected light spectra through GlobES, we calculated the contrast in radiance of the planet at every 5° of its phase in its orbit around the star. We implemented a two-stream approximation to model the angular dependence of aerosol scattering with two Legendre polynomials to approximate the phase function. For each phase's emission and reflected spectrum, we then took the average of the contrast values between 15 µm and 21 µm. We chose this wavelength band because thermal emission is more receptive at the mid-infrared, and because it corresponds to JWST's Mid-Infrared Instrument (MIRI) F1800W imaging filter, which has an average photo conversion efficiency (PCE) of ~0.31 (Bouchet et al. 2015). For clarity purposes, the phase curves are shown not to drop to zero at secondary eclipse (phase of 0), even though the planet would be behind the star. Note that in the phase curves presented in this work, transit occurs at the phase of 180, contrary to the phase-related definitions that other works may use (e.g., Kreidberg et al. 2019).

3. RESULTS

3.1. *Climate States*

In this section we briefly summarize our 3-D climate modeling results. In order to understand our synthetic observables, we must first understand the underlying atmospheric conditions. In Table 3, we describe the basic configuration and climatological properties from our 20 simulations. In Figures 1, 2, and 3, we show vertical profiles of temperature, water vapor, and cloud condensate taken in a slice along the equator for selected simulations. TOI-700 d is a robust candidate for a habitable world, and can potentially maintain temperate surface conditions and significant fractions of surface liquid water under a wide variety of atmospheric compositions. This should come as little surprise, because TOI-700 d is located in the Habitable Zone (Kopparapu et al. 2013, 2016).

Our 14 aquaplanet cases have global mean surface temperatures that range from 236.7 K to 364.2 K, but all still are technically habitable worlds. In our coldest simulation, 1 bar N_2 "plain" aquaplanet with no CO_2, ~24% of the planet still remains free from ice immediately around the substellar point. The addition of modest amounts of CO_2 and CH_4 appropriate for modern Earth and various Archean Earth atmospheric compositions naturally leads to warmer surface temperatures and increasingly larger fractions of open ocean. Still, even with a relatively strong Archean Earth greenhouse (0.1 bar of CO_2 and 10^{-3} bar CH_4), global mean temperatures remain near ~260 K, with sea ice fractions of over 60%. H_2 can also increase the planetary surface temperature through greenhouse forcing from collision induced absorption with N_2, as proposed by Wordsworth & Pierrehumbert (2013). However, our hydrogen-supporting atmosphere (Case 13) only reached a surface temperature of 267.6 K. In order for a planet with a hydrogen-supporting atmosphere to reach modern-Earth-like surface temperatures, it would require either greater than 10% CO_2 and H_2 in a 1 bar total atmosphere, or increased surface pressures. Yet, if we included photochemistry in our models, the inclusion of H_2 would result in additional warming due to its tendency to consume hydroxyl (OH) radicals produced by the photolysis of H_2O in the atmosphere, allowing for a build-up of the greenhouse gas CH_4 (Arney et al. 2016, 2017; Fauchez et al. 2019) which otherwise would be destroyed by OH.

A denser background N_2 atmosphere can significantly raise global mean temperatures via pressure broadening and lapse rate feedbacks (e.g., Goldblatt et al. 2009). With a 4 bar total atmosphere, an Archean Earth composition could raise global mean temperatures to 307 K, and the planet would be globally ocean-covered. However, with too much atmosphere, TOI-700 d could be rendered too hot for habitability. For an Archean Earth composition with a 10 bar background atmosphere, the global mean surface temperature rises to ~360 K. While still technically habitable with surface liquid water and the possibility for thermophilic life forms, such a hot scenario may mark the practical upper limits on habitable atmospheric compositions

#	Archetype	Surface type	Surface pressure (bar)	Primary atmospheric constituent	Minor constituents, partial pressures (bar)	Rotation	Surface temperature (K)	TOA albedo	Sea ice fraction (%)	Stratospheric water vapor (kg/kg)
1	Plain	aqua	1	N_2	H_2O	synchronous	236.7	0.3968	76.2%	$6.5014e-8$
2	Modern Earth	aqua	1	N_2	H_2O CO_2 (4e-4) CH_4 (1.7e-6)	synchronous	246.7	0.3893	71.2%	$3.605e-7$
3	Modern Earth	land	1	N_2	H_2O CO_2 (4e-4) CH_4 (1.7e-6)	synchronous	232.7	0.2840	N/A	N/A
4	Archean Earth	aqua	1	N_2	H_2O CO_2 (0.01) CH_4 (1.0e-4)	synchronous	258.4	0.3594	66.3%	$7.316e-7$
5	Archean Earth	aqua	1	N_2	H_2O CO_2 (0.1) CH_4 (1.0e-3)	synchronous	263.2	0.3988	62.3%	$2.644e-5$
6	Archean Earth	aqua	1	N_2	H_2O CO_2 (0.1) CH_4 (2.0e-3)	synchronous	263.7	0.3998	61.6%	$3.645e-5$
7	Archean Earth	land	1	N_2	H_2O CO_2 (0.1) CH_4 (1.0e-3)	synchronous	251.5	0.2455	N/A	N/A
8	Archean Earth	aqua	0.5	N_2	H_2O CO_2 (0.1) CH_4 (1.0e-3)	synchronous	256.8	0.3906	67.3%	$5.615e-5$
9	Archean Earth	aqua	4	N_2	H_2O CO_2 (0.1) CH_4 (1.0e-3)	synchronous	307.2	0.317	0	$6.406e-6$
10	Archean Earth	aqua	10	N_2	H_2O CO_2 (0.1) CH_4 (1.0e-3)	synchronous	360.8	0.2452	0	$2.203e-6$
11	Archean Earth	aqua	1	N_2	H_2O CO_2 (0.1) CH_4 (1.0e-3)	2:1 resonant	325.7	0.131	0	$6.095e-6$
12	Archean Earth	land	1	N_2	H_2O CO_2 (0.1) CH_4 (1.0e-3)	2:1 resonant	257.0	0.2547	N/A	N/A
13	H_2-supporting	aqua	1	N_2	H_2O CO_2 (0.1) CH_4 (1.0e-3) H_2 (0.1)	synchronous	267.6	0.394	60.3%	$2.669e-5$
14	Early Mars	aqua	0.5	CO_2	H_2O	synchronous	266.2	0.3572	62.6%	$2.802e-5$
15	Early Mars	aqua	1	CO_2	H_2O	synchronous	284.4	0.3775	0.05%	$2.520e-5$
16	Early Mars	aqua	2	CO_2	H_2O	synchronous	324.3	0.2771	0%	$3.027e-5$
17	Early Mars	aqua	4	CO_2	H_2O	synchronous	364.2	0.2214	0%	$2.857e-4$
18	Early Mars	land	1	CO_2	none	synchronous	258.9	0.2304	N/A	N/A
19	Early Mars	land	4	CO_2	none	synchronous	302.3	0.2165	N/A	N/A
20	Early Mars	land	10	CO_2	none	synchronous	353.5	0.2310	N/A	N/A

Table 3. Global mean climatological properties for each of our simulations. By definition, sea ice fraction and stratospheric water vapor or not applicable for desiccated land planet cases. The stratospheric water vapor is taken at the model top, 0.01 mbar. All quantities given are the global and temporal mean.

for TOI-700 d. CO_2 dominated atmospheres, such as those expected for a habitable early Mars, can also produce broadly habitable conditions for ocean-covered planets. With 1 bar of CO_2, the global mean surface temperatures stabilize at a pleasant 284 K, and only a trace amount of sea-ice is present. Yet with a 4 bar CO_2 dominated atmosphere, the global mean temperature reaches ~364 K, our warmest simulation. Note that none of our climates exist in a classical moist greenhouse state. Even for our warmest climate states, with $T_S > 360$ K, stratospheric water vapor remains no greater than 10^{-4}, as seen with the 4 bar CO_2 simulation.

Assuming TOI-700 d is in synchronous rotation, the rotation period of the planet is 37.43 days, making it a slow rotator (Haqq-Misra et al. 2018). On slowly rotating aquaplanets, strong upwelling motions tend to drive the formation of thick substellar clouds (Figure 3), resulting in elevated planetary albedos. Note that the "Modern Earth" aquaplanet, the "Archean Earth" 1 bar aquaplanet, and the "Early Mars" 0.5 and 1 bar aquaplanet cases all have planetary albedos between 0.35 and 0.4, caused primarily by substellar clouds. For thicker and hotter atmospheres, however, the planetary albedo begins to drop due to increased water vapor in the atmosphere (Figure 2) and subsequent near-IR absorption of incoming stellar radiation. Our model predicts that for a synchronously rotating ocean-covered TOI-700 d, planetary albedos near ~0.2 correspond to surface temperatures approaching ~360 K. However, if TOI-700 d is in spin-orbit resonance, the albedo could be significantly lower and yet have a lower surface temperature (~326 K).

We have also included a test case where we assume that TOI-700 d is in a 2:1 spin-orbit resonance. In this case the planetary rotation rate is halved. The substellar point is no longer fixed with respect to the planet surface, and significant changes occur to the planet's general circulation (e.g., Haqq-Misra et al. 2018). If in a 2:1 resonance, TOI-700 d would experience significantly stronger eastward winds that advect both water vapor and clouds east of the substellar point. This phenomenon can be clearly seen in Figures 2 and 3. Because the cloud deck is shifted east of the substellar point, the western part of the substellar hemisphere becomes relatively free from clouds, exposing more ocean. Ocean has a much lower albedo than clouds, thus the planetary albedo drops considerably to 0.131 in this case, and the surface temperature warms by more than 40 K compared to a synchronous rotator with the same atmospheric composition.

We have also explored several desiccated land planet scenarios. These cases as simulated are technically not habitable worlds because water has been effectively removed from the planet. However, land-covered exoplanets need not actually be fully desiccated. They could have polar, night-side, or sub-surface reservoirs of water that could drive weak hydrological cycles and support locally habitable conditions at the cold traps (Abe et al. 2011; Kodama et al. 2015). The global mean surface temperatures for desiccated planets are generally 10 to 20 K lower than for aquaplanets of the same configurations, due to the absence of any water vapor greenhouse effect. However, for dry synchronously rotating land planets, the day-to-night temperature differences can be severe (Figure 1).

For Figures 1, 2, and 3 we show a longitudinal slice around the equator, instead of zonal-mean results for instance, because the climates of slow and synchronous rotators are more aptly described by their day-to-night asymmetries, and because it allows us to highlight the terminator regions of the planet. The vertical dotted lines in each panel mark the terminators. Longitudinal variations in temperature and atmospheric compositions inform us about phase-dependent emission and reflection light curves. Meanwhile, the atmospheric properties at the terminators are relevant for transmission spectroscopy. For all of our simulated cases, the stratospheric temperature above ~1 mbar remains near 180 K regardless of the specific atmospheric composition, surface temperature, and surface pressure. Consequently, for habitable-type atmospheres, the region of the atmosphere probed by transmission spectroscopy does not vary considerably (Figure 1). However, water vapor and clouds do indeed vary substantially between cases, depending on the surface pressure, temperature, and rotation state. In Figures 2 and 3, we omit land planet cases because by definition they have no water and thus no clouds. Warmer climates tend to have more water vapor throughout the atmosphere, and are also cloudier. While high-altitude clouds located along the terminators can obscure transmission spectra (e.g., Fauchez et al. 2019; Suissa et al. 2019), day-to-night asymmetries or phase shifts in clouds could possibly be inferred from thermal emission phase curves and thus give us clues about a planet's circulation and climate state (Yang et al. 2013; Haqq-Misra et al. 2018). The remainder of this paper is devoted to exploring how we may interpret transmission spectra and thermal emission phase curves in the context of three-dimensional cloudy atmospheres, and whether these climate states can be observed with current and future instruments.
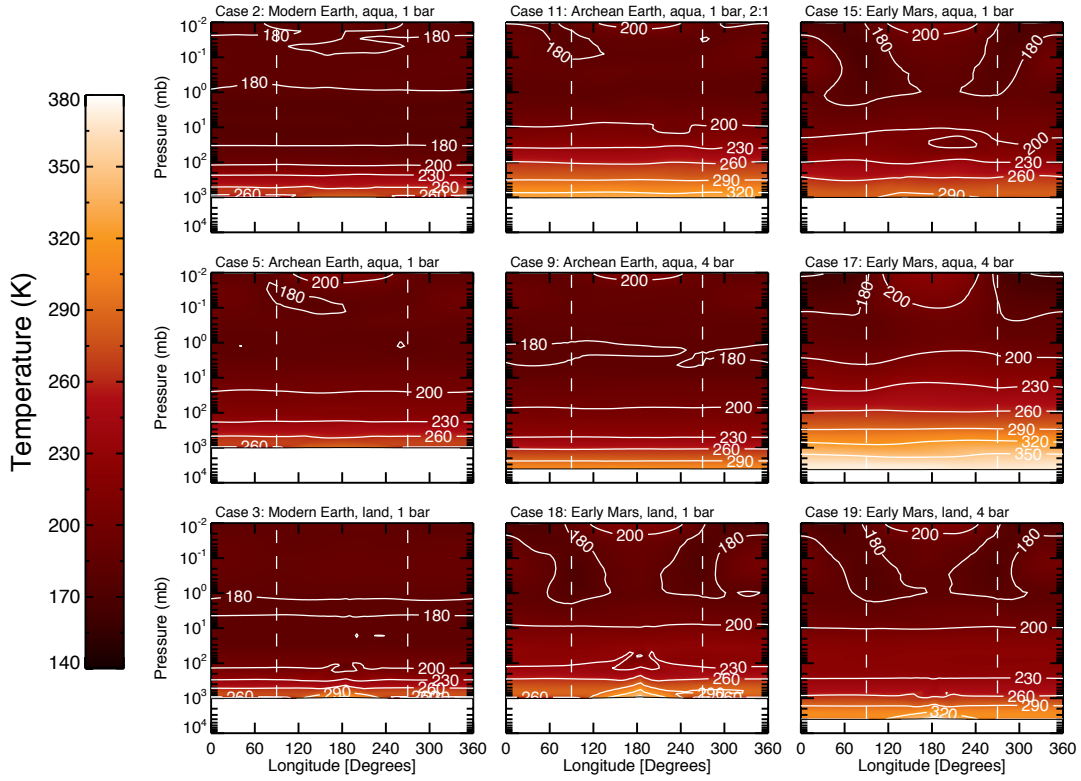
Figure 1. Vertical temperature profiles taken along the equator from 9 characteristic cases. The substellar point is located at 180 degrees. The vertical dashed lines mark the terminators. Despite varying surface pressures and temperatures, stratospheric temperatures are remarkably similar, hovering at ~180 K.
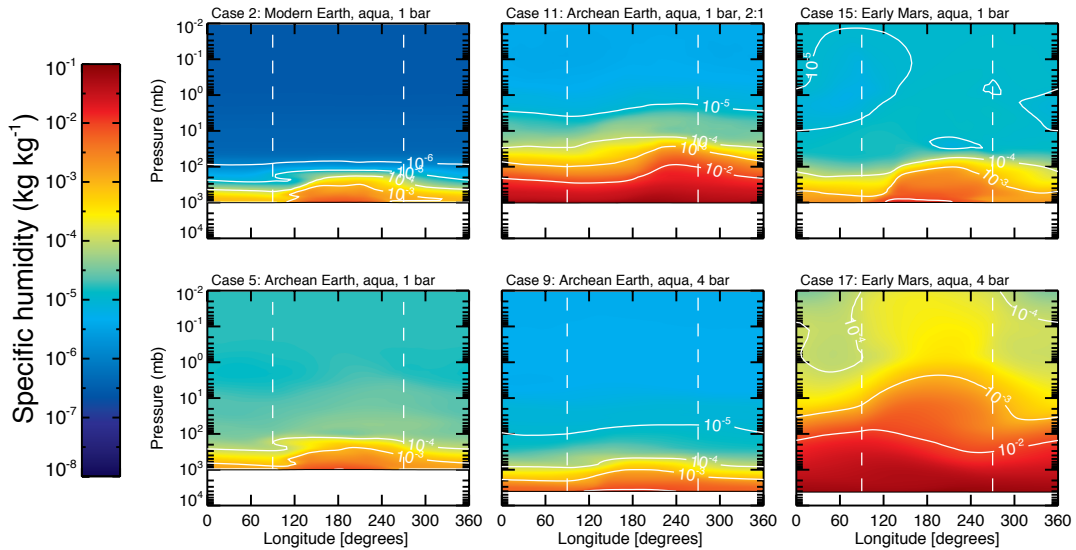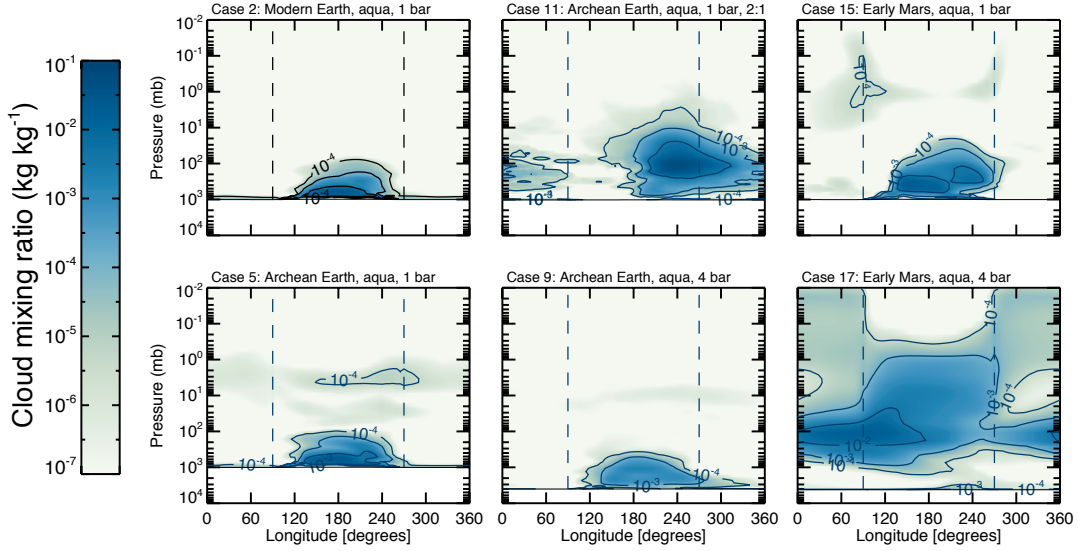

Figure 2. Vertical profiles of water vapor taken along the equator. Same as Figure 1 except dry cases have been omitted. The substellar point is located at 180 degrees. The vertical dashed lines mark the terminators.

Figure 3. Vertical profiles of cloud water taken along the equator. Same as Figure 1 except dry cases have been omitted. The substellar point is located at 180 degrees. The vertical dashed lines mark the terminators.

3.2. *Transmission Spectra*

We present the synthesized transmission spectra for our simulations in Figures 4, 5, 6, and 7. Some prominent features visible in our spectra are the 2.7 μm, 4.3 μm and 15 μm CO_2 features, the 3.4 μm and 7.6 μm CH_4 features, the 1.1 μm, 2.4 μm and 6 μm water bands and the 4.3 μm N_2-N_2 CIA.

In Figure 4, we compare transmission spectra for different atmospheric compositions. We show a spectrum of each atmospheric composition archetype: "Modern Earth", "Archean Earth", and "Early Mars" compositions, as well as the "plain" aquaplanet and "hydrogen-supporting" atmosphere. All cases displayed in Figure 4 are ocean-covered and have a surface pressure of 1 bar. The plain aquaplanet, void of any atmospheric constituents and spectral features apart from N_2 and H_2O, has a very shallow spectrum. Its 6 μm H_2O feature has a depth less than 1 ppm, consistent with that expected for an Earth-sized planet synchronously rotating a ~3500 K star (Suissa et al. 2019; Komacek et al. 2019a). Without CO_2 in its atmosphere, the 4.3 μm N_2-N_2 feature can be seen, indicative of a N_2 dominated atmosphere. For the Modern Earth and Archean Earth simulations, although both cases share the same background N_2 pressure of 1 bar, the continuum is higher in the spectrum for the Archean Earth aquaplanet. This is due to the higher concentration of CO_2, which results in more warming and hence more cloud formation. Clouds dictate where the continuum lies, as they block any incoming stellar radiation from penetrating into lower areas of the atmosphere. Note that the 15 μm CO_2 feature is larger for the Archean Earth case, again because of a higher CO_2 abundance. Although the Early Mars simulation has the most CO_2 in its atmosphere, it has both a smaller 15 μm CO_2 feature and a lower continuum than the Archean Earth case. While the Early Mars case does experience substantial warming (it has the highest global surface temperature out of all the simulations in Figure 4), it has large "cold lobes" in the terminator regions of the upper atmosphere, as can be seen in Figure 1, Case 15. As the terminator is the region of the planet that transmission spectroscopy is sensitive to, the Archean Earth case has a higher continuum because its terminator regions are warmer. Keeping surface pressure and surface-type (i.e., ocean-covered) constant, it is the hydrogen-supported (10% H_2) atmosphere whose spectrum has the highest continuum and the largest 15 μm CO_2 feature. The hydrogen-supported atmosphere is identical to the Archean Earth composition, except 0.1 bar of N_2 is replaced with H_2. A planet with 10% of its N_2 replaced by H_2 has a larger scale height; thus the spectral features for the hydrogen-supported simulation are larger than those of the Archean Earth case. In addition, the continuum is higher for the spectrum of the hydrogen-supporting planet because it is warmer; as detailed in Section 3.1, H_2 collisions with N_2 produce a warming effect that is absent in the Archean Earth case.

In Figure 5, we demonstrate the effect that varying background pressures have on the transit spectra. In general, the continuum level for the relative transit depth rises with increasing pressure, as can be seen distinctly in the first panel of Figure 5. This is because for higher surface pressures, the lower atmosphere is denser, rendering it more opaque to infrared radiation.
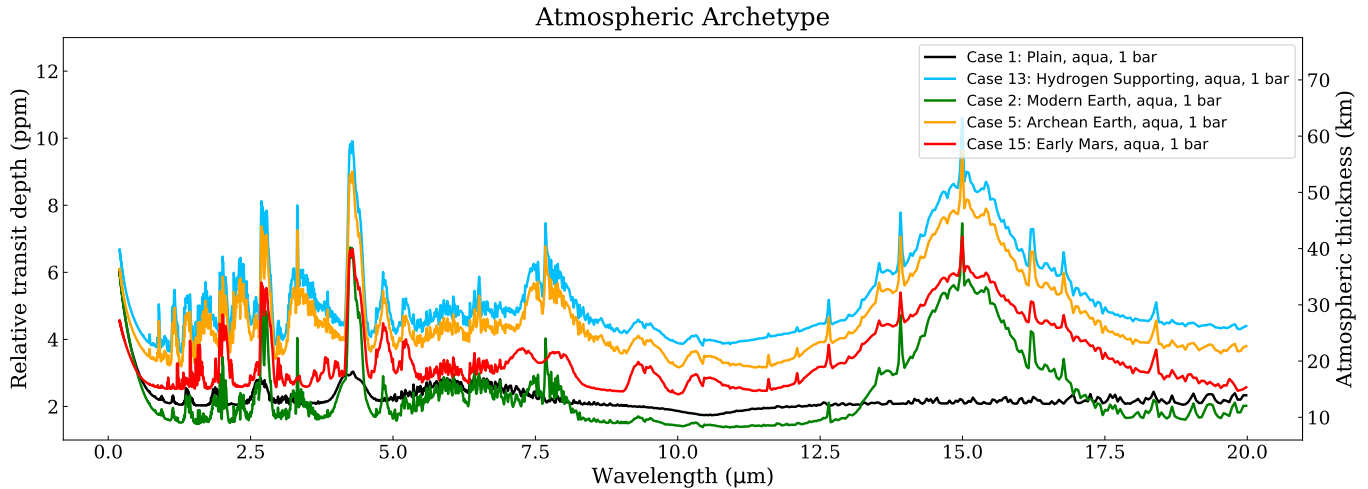
Figure 4. Comparison of transmission spectra for different atmospheric archetypes. All simulations shown here are ocean-covered and have a surface pressure of 1 bar. The spectrum for the "hydrogen-supporting" atmosphere (10% H_2) has both the highest continuum and the largest 15 μm CO_2 feature.

The continuum level therefore rises to higher altitudes where the opacity is reduced. In addition, higher atmospheric pressure leads to more atmospheric refraction, also contributing to the increase in the continuum level. For all of the aquaplanet cases, clouds are present in the atmosphere. They partially or completely block the incoming stellar radiation, situating the continuum level above the cloud deck. Higher pressure atmospheres can further augment the production of high-altitude clouds by inducing a greenhouse warming effect due to pressure broadening, allowing for a warmer planet where more clouds form and push the continuum higher. In the second panel of Figure 5, the continuum level for the 4 bar CO_2 atmosphere is at ~40 km, substantially higher than any of the lower pressure cases. The dramatic rise in the continuum for this particular simulation is not just due to the opaqueness of its lower atmosphere or pressure broadening. Note that in the 10 bar N_2 case in the top panel of Figure 5, clouds do not push the continuum level as high. This is because, while N_2 pressure broadening does produce a moderate greenhouse warming (Wordsworth & Pierrehumbert 2013; Goldblatt et al. 2009), it pales in comparison to the warming produced by a potent greenhouse gas such as CO_2, even if the N_2 atmosphere has a higher pressure than the CO_2 dominated planet. Since both the 10 bar N_2 and the 4 bar CO_2 simulations are ocean-covered, the simulation that experiences a greater greenhouse warming and an increased production of high-altitude water vapor clouds will have the highest continuum level. For the desiccated planet cases in the bottom panel of Figure 5, an increase in the CO_2 pressure results in the increase of the continuum only due to the atmospheric refraction, as there are no clouds.

Clouds not only affect the continuum level, but the depths of the individual transit spectral features themselves. For example, in the middle panel of Figure 5, one can notice the rapid decrease in the relative transit depth of the 15 μm CO_2 feature as the CO_2 pressure increases. This is again due to the "masking" of water clouds formed from the increase in the greenhouse warming.

The addition of varying amounts of N_2 as a background gas introduces features that could be indicative of a dense nitrogen atmosphere (Komacek et al. 2019a). For instance, the top panel in Figure 5 shows N_2 pressure broadening features just below 2.5 μm and around 3 μm, both of which are absent in the CO_2 dominated atmospheres in the middle and bottom panels. Even as little as 0.5 bar of N_2 seems to be large enough for these features to appear in the transmission spectrum. It should be noted that nitrogen is the primary (for Earth) or the second most abundant gas (for Venus and Mars) in the terrestrial planetary atmospheres in our Solar System. If this is true for exoplanetary atmospheres as well, N_2 pressure broadening features could be a marker for such atmospheres. In addition, N_2-N_2 collision-induced absorption (CIA) at ~4.3 μm, in the wing of the CO_2 absorption feature, can be another indication of a N_2-rich atmosphere as shown by Schwieterman et al. (2015). In the absence of CO_2, this signal could be substantially larger, especially for planets with significant H_2 mixing ratios.

In Figure 6, we compare the spectral feature differences between ocean-covered worlds and desiccated planets. In each panel it is apparent that the aquaplanet has a higher continuum level as well as reduced feature depths compared to its land-covered counterpart, due to the presence of high-altitude water vapor clouds. Likewise, the spectra for the ocean-
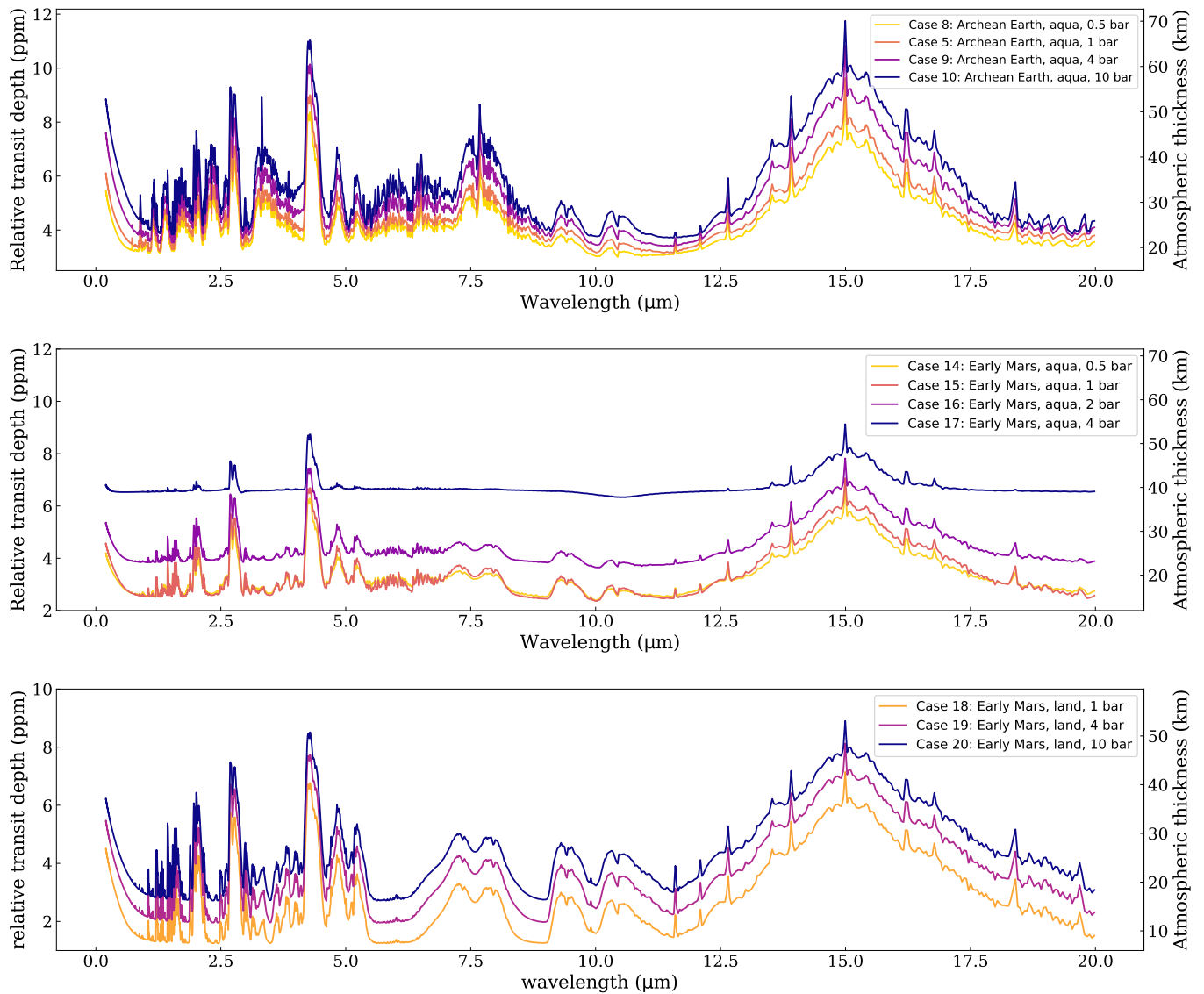
Atmospheric Pressure

Figure 5. Comparison of synthesized transmission spectra for different atmospheric pressures. "Archean Earth" aquaplanets of different surface pressures are presented in the top panel, "Early Mars" aquaplanets in the middle panel, and "Early Mars" desiccated planets in the bottom panel. In general, as the pressure increases, the continuum level of the spectrum increases as well.

covered planets include water vapor features, such as the 6 μm feature, which are absent in the dry cases. This absence reveals that the dry 1 bar "Archean Earth" case has enough methane in its atmosphere to have a 6 μm CH_4 feature, which could be useful in identifying an atmosphere as dry, haze-free and methane-rich. To distinguish between desiccated planets that have "Modern Earth"-like and "Archean Earth"-like compositions, identifying CH_4 features can be a key observational constraint. The strength of the CH_4 features increases with the increase of the CH_4 abundance in the atmosphere, as can be seen by comparing the heights of the ~3.7 μm or the ~7.5 μm features between the "Archean Earth" and "Modern Earth" cases. Note that in our CO_2 dominated "Early Mars" atmospheres, CH_4 is not specified in the atmosphere, because the source fluxes for species such as methane in an early Mars would be low, and thus is not present in their associated transmission spectra. Figure 6 also indicates that, while the 15 μm CO_2 feature, irrespective of its abundance, may betray the presence of an atmosphere, its detection alone cannot specify an atmospheric archetype or surface condition, because it is prominent in all of the simulated cases (except for the "plain" aquaplanet and the 4 bar CO_2 dominated aquaplanet in the middle panel of Figure 5).
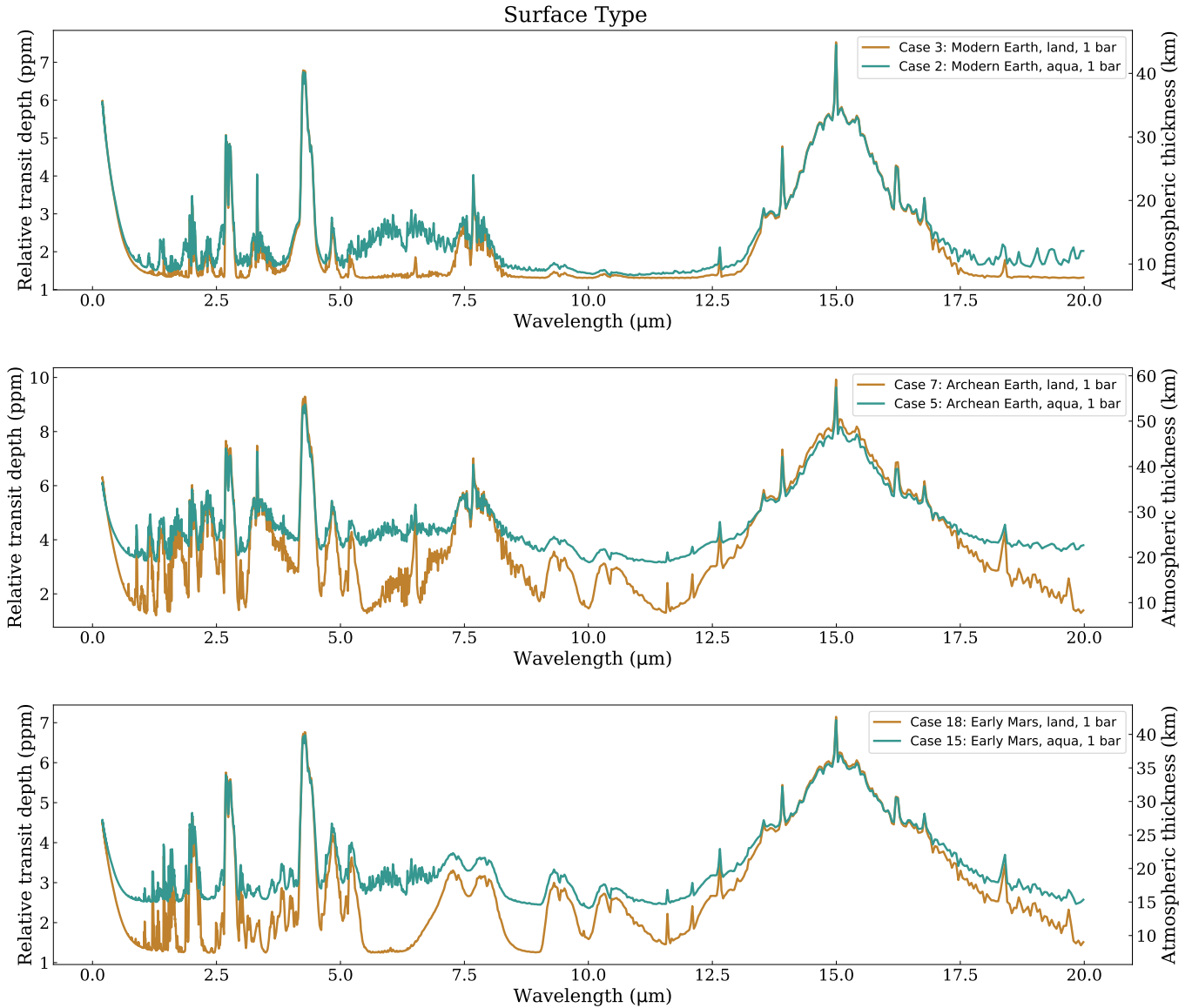
Figure 6. Comparison of the synthesized transmission spectra of aquaplanets to their desiccated counterparts. The ocean-covered planets have higher continuum levels and reduced feature depths due to the presence of clouds.

We highlight the effect that different orbit phenomena have on transmission spectra in Figure 7. The "Archean Earth" aquaplanet in a 2:1 rotation:orbit resonance has a higher continuum and smaller spectral feature depths than its synchronously rotating counterpart does, although the atmospheric compositions are the same. This is because, as seen for Case 11 in Figure 3, the resonant simulation experiences an eastward shift of large clouds. These clouds on the eastern side of the planet breach and heavily obscure the terminator region, the area of the planet sensitive to transmission spectroscopy. When comparing the "Archean Earth" 1 bar land planet against its resonant desiccated analogue, the transmission spectra (not shown here) are identical due to the lack of the clouds that produce this effect.

A property shared by all of our generated transmission spectra, including those displayed in Figure 5, 6, 7, is that the spectral feature depths are low, with the relative transit depth for the large 15 μm CO_2 feature usually hovering between 4 and 6 ppm (with the exception of the 4 bar CO_2 dominated case, for which the 15 μm CO_2 feature has a depth of ~1 ppm, and the "plain" aquaplanet, which has no CO_2). The implications of these low signals are discussed in Section 4.
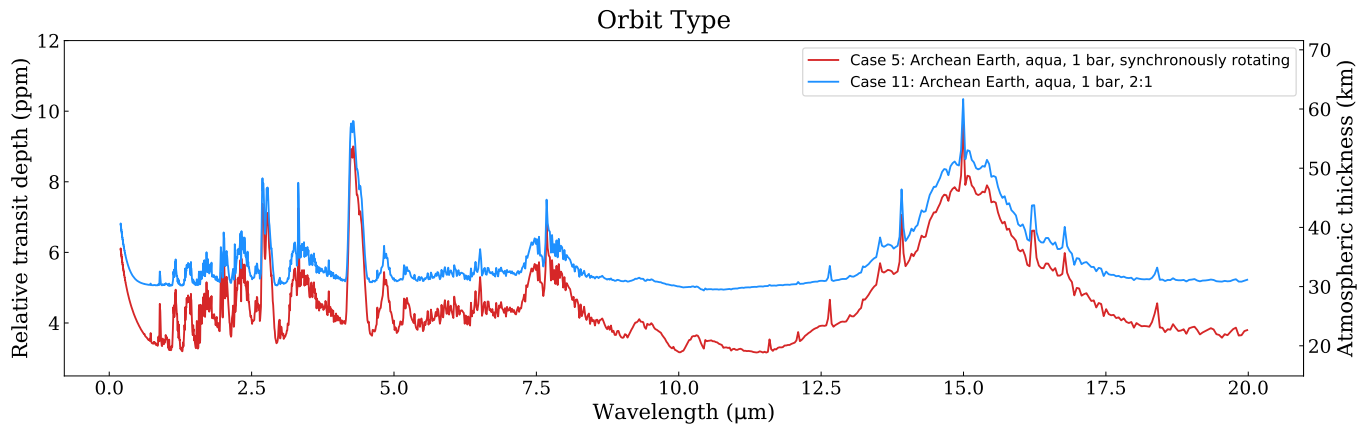
3.3. *Combined Phase Curves*

Figure 7. Comparison of the transmission spectrum of a synchronously rotating "Archean Earth" aquaplanet against its 2:1 spin-orbit resonant counterpart. Although they share the same atmospheric composition, the resonant case's spectrum has a higher continuum and diminished features due to its eastern cloud formation.

In Figures 8, 9, and 10, we present combined-light (thermal emission and reflected light) phase-dependent spectra (left panel) and integrated broadband phase curves (right panel) for different atmospheric compositions of TOI-700 d. Note that for the broadband phase curves, a phase of 180° is the transit and 0° is the secondary eclipse. The integrated fluxes are from the 15−21 μm bandpass, where the thermal emission from the planet is dominant. The morphology of a broadband phase curve is driven by longitudinal variations, which result from both the atmospheric composition and dynamics. For the aquaplanet cases, the shape of the phase curve traces the extent of the cloud cover on the planet. This aspect highlights the advantage of using a 3-D climate model, where the global cloud distribution can be self-consistently simulated to assess its effect on observables.

Figure 8 shows the distinct variation in both the spectrally resolved and broadband phase curves between ocean-covered (top) and desiccated (bottom) planet configurations, assuming 1 bar "Modern Earth" atmospheric composition for TOI-700 d. Several interesting features can be noted comparing the two cases (Cases 2 and 3 in Table 3). The land planet simulation has an unmistakable minimum at the transit phase (180°). Meanwhile, the aquaplanet model has a mostly flat phase curve, with minima at the secondary eclipse phases (0° and 360°), and perhaps a very slight dip close to transit. The morphology of the phase curve for the desiccated planet effectively illustrates that there is a larger day-to-night contrast in the desiccated planet case compared to its flat aquaplanet counterpart. Without water vapor to efficiently transport heat and without clouds to redirect escaping flux back to the surface, the locked dayside of the land planet receives and reflects most of the available flux from the host star. The land planet's phase curve distinguishes itself from that of a bare rock as it has a lower amplitude than what is empirically expected for an atmosphere-less planet (Koll & Abbot 2015), due to the existing heat distribution of the atmosphere. For the aquaplanet case in Figure 8, the minima at the secondary eclipse are due to the substellar clouds, which inhibit the escape of long-wave thermal radiation. As there are no clouds in the land planet case, no such reduction can be seen in the broadband phase curve near the secondary eclipse.

The phase-dependent combined-light spectra in Figure 8 (left panel) also show distinct variations, particularly in the near-IR (∼0.8−3 μm) for the aquaplanet case, where water vapor absorption can be identified. In both of these cases, the strong 15 μm CO_2 absorption feature stands out, betraying the presence of an atmosphere. While transit observations can potentially detect the presence of CO_2 in the atmosphere in the near-IR part of the spectrum, thermal emission spectra can also be used to verify the existence of an atmosphere.

In Figure 9 we highlight the effect that rotation has on phase curve morphologies. The top panel is a synchronously rotating 1 bar aquaplanet with an "Archean Earth" composition (Case 5 in Table 3). The bottom panel is the aquaplanet simulation with the same atmospheric properties, except in a 2:1 rotation:orbital resonance (Case 11). The synchronously rotating case has a similar phase curve morphology as that of the "Modern Earth" aquaplanet displayed in Figure 8. However, the "Archean Earth" is slightly flatter, corresponding to less of a day-to-night temperature variation, due to the increased amount of CO_2 warming in the atmosphere. Meanwhile, the 2:1 resonant case in Figure 9 dips when the east side of planet comes into view. As can be seen in the cloud profile for this case in Figure 3, there is heavy cloud cover asymmetrically skewed towards the east side of the planet. The eastern clouds block the outgoing infrared radiation, resulting in a low contrast of thermal emission at
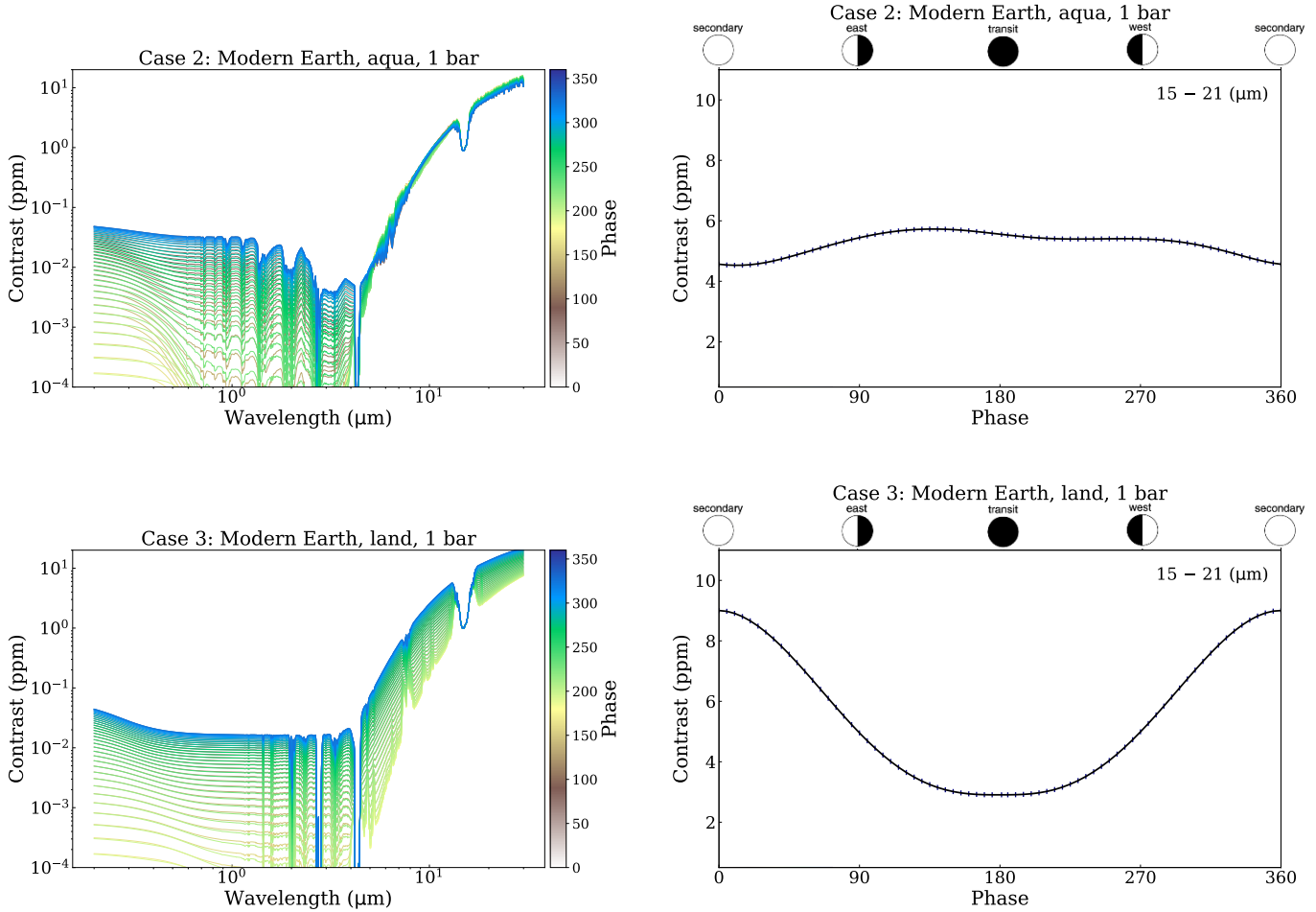
Figure 8. Combined-light phase-dependent spectra (left panel) and integrated broadband phase curves (right panel) for the Modern Earth aquaplanet (top) and the Modern Earth desiccated planet (bottom). Transit occurs at 180°. The integrated fluxes for the phase curves are 15–21 μm.

90°. As the planet approaches transit and beyond, the thermal emission increases due to the westward dwindling of clouds. There is no minimum of thermal emission at transit, because the planet is not tidally locked, and thus the longitudinal distribution of temperature is more or less uniform. The only factor that contributes to the variations in the resonant case's phase curve is the distribution of clouds.

We overlay synthesized phase curves for the majority of our simulations in Figure 10, which is divided into aquaplanets (top panel) and desiccated planets (bottom panel). The 10 bar "Archean Earth" simulation (Case 10) has the highest contrast (~10 ppm) due to the combination of its high temperatures and relatively mild cloud coverage. Although the 4 bar "Early Mars" planet (Case 17) is our hottest simulation, it has a substantial amount of clouds (see Figure 3), and thus has a lower-contrast phase curve than the 10 bar "Archean Earth" planet. The bottom panel of Figure 10 demonstrates that the "Modern Earth" desiccated case not only has the largest day-to-night temperature differences, but also has the second largest contrast of our simulated phase curves (~9 ppm). All of our simulations yield maximum variation below 10 ppm, with the average maximum contrast being ~6 ppm. The observability prospects for these low signals are discussed in Section 4.

4. DISCUSSION

In this paper, we have explored possible habitable climates for the first Habitable Zone Earth-sized planet discovered by the TESS mission: TOI-700 d (Gilbert et al. submitted, Rodriguez et al. submitted). We have presented synthesized transmission spectra, phase-dependent combined-light spectra, and integrated broadband phase curves for the planet, based on
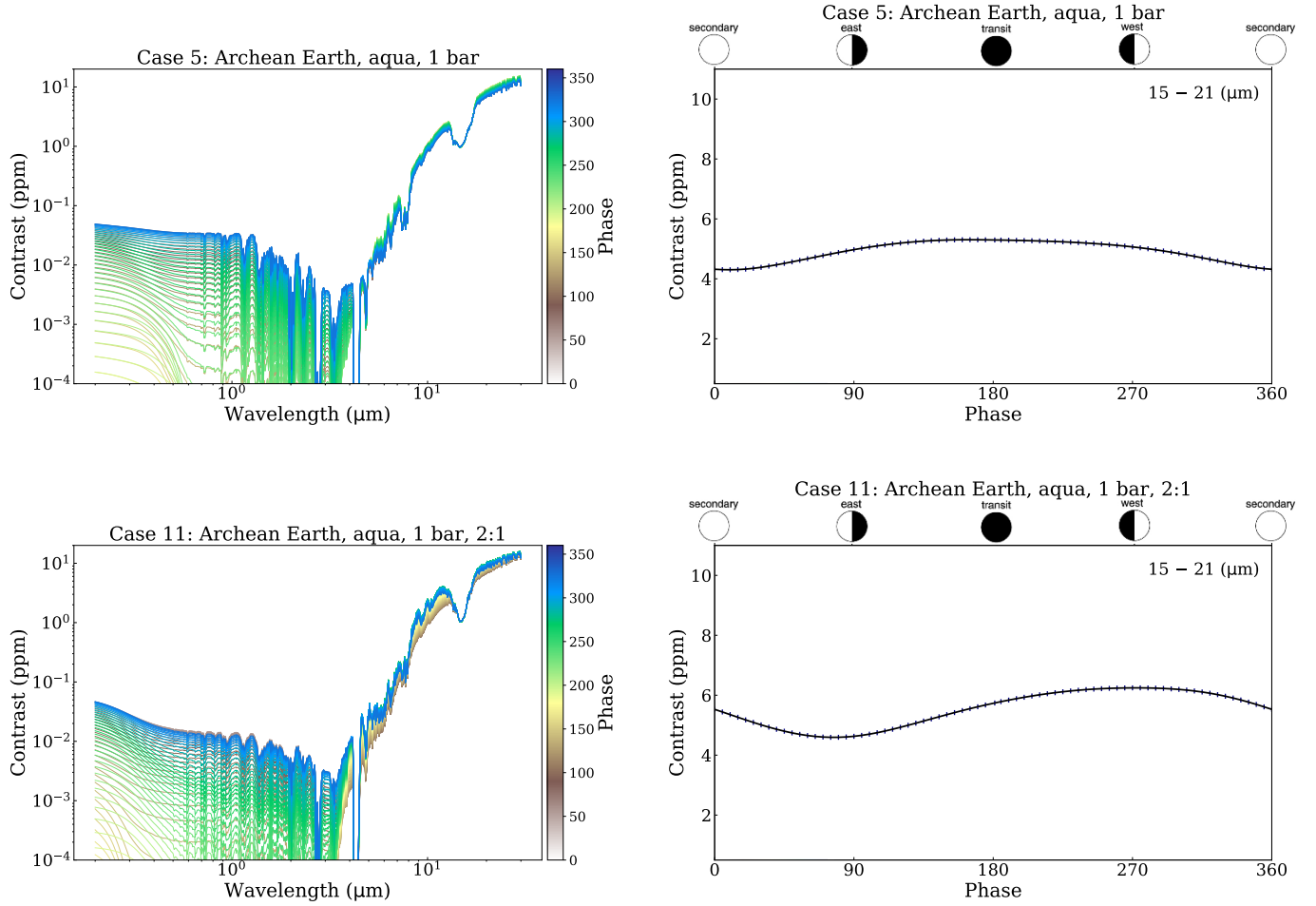
Figure 9. Combined-light phase-dependent spectra (left panel) and integrated broadband phase curves (right panel) for a synchronously rotating 1 bar Archean Earth aquaplanet (top) and its 2:1 spin-orbit resonant aquaplanet counterpart (bottom). Transit occurs at 180°. The integrated fluxes for the phase curves are 15−21 μm.

ExoCAM GCM simulations of a diversity of climate conditions. Receiving ~0.86 S_0 from a ~3500 K star makes TOI-700 d a robust candidate for a habitable world. Due to its long-period orbit, TOI-700 d in some ways may be better suited for habitability than TRAPPIST-1 e and Proxima Centauri b, both of which are markedly colder and receive only ~0.6 S_0. As outlined in Section 3.1, for the cases where we assume the planet is an ocean world and in synchronous rotation, we find that the planet still maintains habitable conditions for a diverse set of surface pressures and atmospheric conditions, with our coldest simulation (the "plain" aquaplanet) still maintaining ~24% of open ocean. We use the 10 bar "Archean Earth" and 4 bar "Early Mars" cases to mark the upper limits of habitability for the simulations we explore here for TOI-700 d. For desiccated planets, the global mean surface temperatures are generally 10 to 20 K lower than for aquaplanets of the same configurations because of the absence of any water vapor. For the non-synchronous, 2:1 spin-orbit resonance aquaplanet, we find that the surface temperature warms by more than 40 K compared to a synchronous case with the same atmospheric composition. We also have presented several ways to disentangle the different climate states from the observables we synthesized. It may be possible, for example, to distinguish a dry, haze-free, methane-rich atmosphere, as well as discern between N_2 and CO_2 dominated atmospheres. The distinctions between phase curve morphologies for desiccated and ocean-covered worlds, as well as a synchronously rotating aquaplanet and a 2:1 resonant aquaplanet are also quite clear. Our observables show that the presence of a CO_2-containing atmosphere can be easily discernible via CO_2 spectral features, provided our instruments capabilities allow it (see Section 4.2 below).
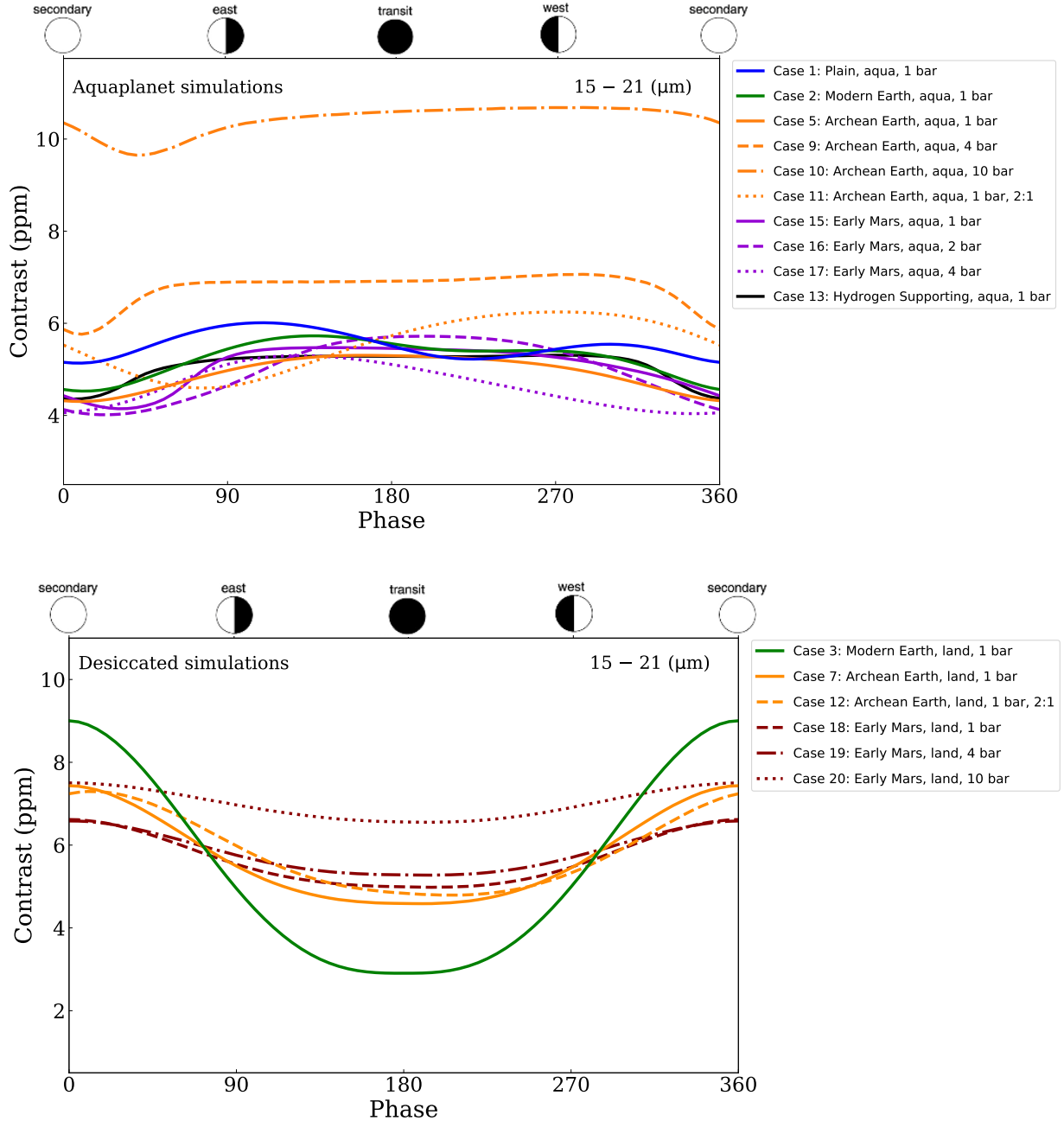
Figure 10. Phase curves for the majority of our simulations in this work. Aquaplanets are shown in the top panel; desiccated planets are shown in the bottom panel. Transit occurs at 180°. The integrated fluxes for the phase curves are 15−21 µm.

4.1. *Atmospheric Retention*

Although we simulate many different climatological scenarios, it is an open-ended question as to whether or not TOI-700 d has suffered from atmospheric loss. The host star is a quiet early M dwarf with an age estimate of >1.5 Gyr (Gilbert et al. submitted). Recent studies have pointed out that lower mass stars undergo an extended phase of high-luminosity pre-main sequence evolution as they fuse hydrogen into helium in their cores (Ramirez & Kaltenegger 2014; Luger & Barnes 2015; Tian & Ida 2015). For a G-dwarf star like our Sun, this pre-main sequence phase lasts only ~50 Myr (Baraffe et al. 2015), but the stage can last anywhere from ~100 Myr to ~1 Gyr for early and late M-dwarfs, respectively. TOI-700 is an early M dwarf with a mass estimate of 0.416 M$_\odot$, and so it should have a relatively short high-luminosity pre-main sequence evolution, perhaps
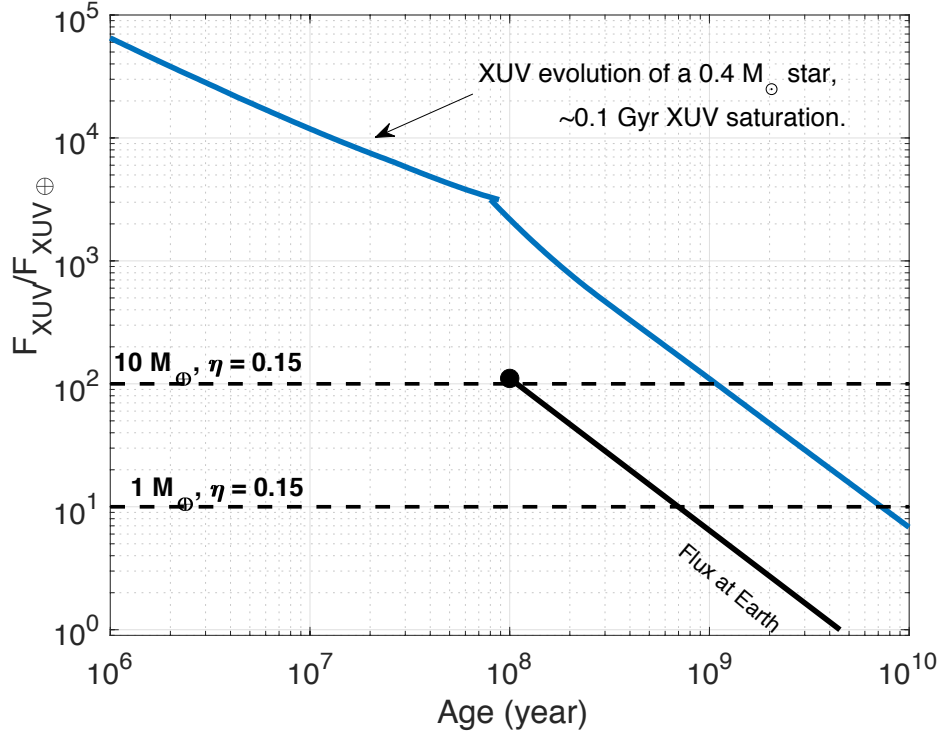
Figure 11. Incident XUV ($1 - 1000$ Å) flux evolution normalized to the present Earth value (4.64 ergs·s^{-1}·cm^{-2}) on TOI-700 d from a star with a mass equivalent to that of its host star (blue curve). An XUV saturation time of ~0.1 Gyr is assumed. The flux evolution on Earth from a Sun-like star is also shown (black solid), and the black dot represents the earliest time Ribas et al. (2005) have data for solar-type stars. The horizontal dashed lines show the threshold XUV limit for the "blowing off" of an atmosphere on a 1 M$_\oplus$ and 10 M$_\oplus$ planet above which the escape of the atmosphere is dominated by the hydrodynamic wind, assuming heating efficiencies of 0.15. Depending upon the age of the system, TOI-700 d may be below the threshold for the blow-off of its atmosphere.

only ~200 Myr (Luger & Barnes 2015). For TOI-700, the variation in the bolometric luminosity itself is less than an order of magnitude while entering into the main sequence, while a late M-star spectral type (like TRAPPIST-1) experiences several orders of magnitude variation in the latter case. This could potentially be advantageous in terms of retaining an atmosphere for the terrestrial-sized planet in the HZ, TOI-700 d.

However, while TOI-700 is a quiet M dwarf, this stellar type is more active than solar-type stars (Scalo et al. 2007), with X-ray and UV radiation (XUV, $1 - 1000$ Å) particularly excessive during the young, pre-main sequence period of M-dwarf stars. XUV radiation can lead to atmospheric escape, stripping the atmosphere of a planet in the HZ (Watson et al. 1981; Lammer et al. 2003, 2009, 2013; Yelle 2004; Erkaev et al. 2007, 2013; Tian 2009; Owen & Jackson 2012). In Figure 11, we compare the incident XUV radiation over time on TOI-700 d using a star with an equivalent mass of TOI-700 (solid blue line) based on the evolutionary path for XUV radiation from Ribas et al. (2005). We assume a XUV "saturation" timescale (i.e, the XUV luminosity is saturated, and remains constant for 0.1 Gyr, after which it decreases) of ~0.1 Gyr. For comparison, the XUV flux on Earth from the Sun is also shown (solid black line). The solid filled circle is the earliest time for which Ribas et al. (2005) have integrated XUV flux estimates for solar type stars in the wavelength interval $1 - 1180$ Å (see their Table 4, entry for EK Dra). We also show the threshold XUV limit for the "blowing off" of an atmosphere on a 1 M$_\oplus$ and 10 M$_\oplus$ planet (dashed horizontal lines), above which the escape of the atmosphere is dominated by the hydrodynamic wind. We assume for heating efficiencies of 0.15. The heating efficiency η is defined as the percentage of incoming XUV energy that is transferred locally into heating of the gas (Erkaev et al. 2013). Given the above assumptions, Figure 11 indicates that Earth-mass planets around TOI-700-type stars may be in the blow-off regime for several billion years, resulting in the loss of their primary atmospheres. TOI-700 d is a planet with a mass that is likely less than 5 M$_\oplus$. While a mass larger than that of the Earth could moderately reduce the atmospheric blow-off time assuming the same heating efficiency, if the planet formed with its current size, it is still likely that the planet may have lost its primordial atmosphere.

Although there is a possibility that a primordial atmosphere may have been stripped off due to the above mentioned high luminosity pre-main sequence evolution of the host star, secondary atmospheres may build up past this phase through volcanic outgassing (Wordsworth & Pierrehumbert 2013; Driscoll & Bercovici 2014). Tectonic activity (either through tidal forces, or similar to the Earth) may facilitate an efficient water cycling between the interior and the surface, potentially sustaining oceans on the surface of the planet (Sandu et al. 2011; Cowan & Abbot 2014; Schaefer & Sasselov 2015; Komacek & Abbot 2016). The survival of oceans on the surface of an M-dwarf planet depends upon the stellar UV activity, and the corresponding escape of hydrogen into space. Although we did not include the effect of photochemistry for our climate simulations in this work, other studies have used either a self-consistent GCM-photochemistry model to directly simulate the resultant H_2 mixing ratios due to stellar activity (Chen et al. 2019), a 1-D photochemistry model coupled to a GCM (Badhan et al. 2019), or simply an estimate of the ocean-loss timescale based on the model top water vapor mixing ratios from solely the GCM climate outputs (Kopparapu et al. 2016; Wolf & Toon 2015). All of these studies estimate the water-loss rates assuming diffusion-limited escape rates of hydrogen (Hunten 1973). The general conclusion seems to be that around inactive stars, the water-loss is more resilient to hydrogen escape, with ocean survival times exceeding ~10 Gyr (Bolmont et al. 2017).

4.2. *Prospects for Atmospheric Characterization*

As one of the nearest M stars with a known transiting Earth-sized planet in the Habitable Zone, TOI-700 represents a potential target for future observing campaigns to characterize the atmospheres of potentially habitable planets. However, with a stellar radius of 0.41 $R_\odot$, the projected area of TOI-700 is still relatively large compared with more favorable late-type M-star targets; TRAPPIST-1, for example, has a projected size that is 11 times smaller. The transit depth depends linearly on the stellar projected area, and therefore the depth of spectral features in transmission are small - the simulated transmission spectra for all the modeled atmospheres in our study generally have spectral line contrasts that peak at ~6 ppm. Dry planets with thin atmospheres have the largest amplitude phase curves, due to a lack of efficient heat transport, both in peak flux as well as amplitude variation, but even these have maximum planet/star flux contrasts of at most ~10 ppm.

The upcoming launch of the James Webb Space Telescope provides us with our first opportunity to characterize transiting planets across a wide range of wavelengths using a stable space-based platform. However, even the most optimistic scenarios for the noise floor (i.e., the minimum uncertainty on the transit or eclipse depth measurements that can be achieved by JWST due to pseudorandom instrument noise) are 10-20 parts per million (ppm) at 1σ (Greene et al. 2016). Therefore prospects for characterizing TOI-700 d with JWST will most likely be unfeasible, unless the noise floor limit is significantly better than expected. Yet even with a noise floor of ≤ 2 ppm, we would still only be limited to obtaining a constraint on whether the planet has an atmosphere or not (Lustig-Yaeger et al. 2019; Koll et al. 2019; Fauchez et al. 2019). For this reason, we do not perform actual SNR calculations to determine required observing time in this study; however, initial estimates of the number of JWST transits or eclipses needed are in the 100s, and thus would not even fit within the nominal lifetime of the observatory (Rodriguez et al. submitted). In addition, stellar contamination from spots and/or feculae could produce spectral features equal or larger than planetary atmospheric signals at certain wavelengths (Ducrot et al. 2018). Future observatories with ultra-stable instruments for long-baseline time series observations (such as Origins or LUVOIR (Meixner et al. 2019; The LUVOIR Team 2019)) may be designed to achieve this level of precision, but such performance has not yet been demonstrated.

Similarly, directly imaging TOI-700 d will be prohibitively challenging for even the proposed next-generation high-contrast coronographic instrumentation for the ELTs (such as the PCS/EPICS coronograph proposed for the E-ELT, Kasper et al. 2011) or for space-based missions such as the Large Ultraviolet Optical Infrared Surveyor (LUVOIR, Roberge et al. 2019). Imaging the planet from $0.5 - 1\,\mu m$ would require a contrast of $\sim 10^{-8}$ at 5 milliarcsec, which is significantly better than the current requirements baselined for these instruments (Kasper et al. 2011; Roberge et al. 2019). Significant characterization efforts will therefore require future space-based IR interferometer missions such as the proposed LIFE (Large Interferometer For Exoplanets) mission (Quanz et al. 2018).

While the detection threshold of the spectral signals for this particular planet are most likely unfeasible for near-term observing opportunities, the end-to-end atmospheric modeling and spectral simulation study that we have performed in this work is an illustrative example of how global climate models can be coupled with a spectral generation model to assess the potential habitability of any HZ terrestrial planets discovered in the future, as we have done here with the exciting new discovery, TOI-700 d. With more discoveries on the horizon with TESS and ground-based surveys, we hope that this methodology will prove useful for not only predicting the observability of HZ planets but also for interpreting actual observations in the years to come.

Software: ExoCAM (https://github.com/storyofthewolf/ExoCAM), PSG (Villanueva et al. 2018)

REFERENCES

Abe, Y., Abe-Ouchi, A., Sleep, N. H., & Zahnle, K. J. 2011, Astrobiology, 11, 443

Adams, A. D., Boos, W. R., & Wolf, E. T. 2019, ApJ, 157, 189

Allard, F., Allard, N. F., Homeier, D., et al. 2007, A&A, 474, L21

Arney, G., Domagal-Goldman, S. D., Meadows, V. S., et al. 2016, Astrobiology, 16, 873

Arney, G. N., Meadows, V. S., Domagal-Goldman, S. D., et al. 2017, ApJ, 836, 49

Badhan, M. A., Wolf, E. T., Kopparapu, R. K., et al. 2019, The Astrophysical Journal, 887, 34

Baraffe, I., Homeier, D., Allard, F., & Chabrier, G. 2015, A&A, 577, A42

Barnes, R. 2017, Celestial Mechanics and Dynamical Astronomy, 129, 509

Barnes, R., Mullins, K., Goldblatt, C., et al. 2013, Astrobiology, 13, 225

Bolmont, E., Selsis, F., Owen, J. E., et al. 2017, Monthly Notices of the Royal Astronomical Society, 464, 3728

Bouchet, P., García-Marín, M., Lagage, P. O., et al. 2015, PASP, 127, 612

Checlair, J. H., Menou, K., & Abbot, D. S. 2017, ApJ, 845, doi:10.3847/1538-4357/aa80e1

Checlair, J. H., Olson, S. L., Jansen, M. F., & Abbot, D. S. 2019, ApJ, 884, doi:10.3847/2041-8213/ab487d

Chen, H., Wolf, E. T., Zhan, Z., & Horton, D. E. 2019, ApJ, 886, 16

Clough, S. A., Shephard, M. W., Mlawer, E. J., et al. 2005, JQSRT, 91, 233

Cowan, N. B., & Abbot, D. S. 2014, ApJ, 781, 27

Del Genio, A. D., Way, M. J., Amundsen, D. S., et al. 2019, Astrobiology, 19, 99

Dobrovolskis, A. R. 2009, Icarus, 204, 1

Driscoll, P., & Bercovici, D. 2014, Physics of the Earth and Planetary Interiors, 236, 36

Ducrot, E., Sestovic, M., Morris, B. M., et al. 2018, The Astronomical Journal, 156, 218

Erkaev, N. V., Kulikov, Y. N., Lammer, H., et al. 2007, A&A, 472, 329

Erkaev, N. V., Lammer, H., Odert, P., et al. 2013, Astrobiology, 13, 1011

Fauchez, T., Turbet, M., Wolf, E. T., et al. 2019, Geoscientific Model Development Discussions, 2019, 1

Fauchez, T. J., Turbet, M., Villanueva, G. L., et al. 2019, ApJL, in review

Forget, F., Hourdin, F., Fournier, R., et al. 1999, Journal of Geophysical Research: Planets, 104, 24155

Fujii, Y., Del Genio, A. D., & Amundsen, D. S. 2017, ApJ, 848, 100

Goldblatt, C., Claire, M. W., Lenton, T. M., et al. 2009, Nature Geoscience, 2, 891

Gordon, I. E., Rothman, L. S., Hill, C., et al. 2017, JQSRT, 203, 3

Greene, T. P., Line, M. R., Montero, C., et al. 2016, ApJ, 817, 17

Halevy, I., Pierrehumbert, R. T., & Schrag, D. P. 2009, Journal of Geophysical Research (Atmospheres), 114, D18112

Haqq-Misra, J., Wolf, E. T., Joshi, M., Zhang, X., & Kopparapu, R. K. 2018, ApJ, 852, 67

Hourdin, F., Musat, I., Bony, S., et al. 2006, Climate Dynamics, 27, 787

Hunten, D. M. 1973, Journal of Atmospheric Sciences, 30, 1481

Kane, S. R., Kopparapu, R. K., & Domagal-Goldman, S. D. 2014, ApJL, 794, L5

Kang, W. 2019, ApJ, 877, L6

Kasper, M., Gratton, R., Verinaud, C., et al. 2011, in Second International Conference on Adaptive Optics for Extremely Large Telescopes. Online at <A href="http://ao4elt2.lesia.obspm.fr">http://ao4elt2.lesia.obspm.fr</A>, 12

Keller-Rudek, H., Moortgat, G. K., Sander, R., & Sörensen, R. 2013, Earth System Science Data, 5, 365

Kodama, T., Genda, H., Abe, Y., & Zahnle, K. J. 2015, ApJ, 812, 165

Koll, D. D., & Abbot, D. S. 2015, ApJ, 802, 21

Koll, D. D. B., Malik, M., Mansfield, M., et al. 2019, The Astrophysical Journal, 886, 140

Komacek, T. D., & Abbot, D. S. 2016, ApJ, 832, 54

—. 2019, ApJ, 871, 245

Komacek, T. D., Fauchez, T. J., Wolf, E. T., & Abbot, D. 2019a, ApJL, submitted

Komacek, T. D., Jansen, M. F., Wolf, E. T., & Abbot, D. S. 2019b, ApJ, 883, 46

Kopparapu, R. k., Wolf, E. T., Arney, G., et al. 2017, ApJ, 845, 5

Kopparapu, R. k., Wolf, E. T., Haqq-Misra, J., et al. 2016, ApJ, 819, 84

Kopparapu, R. K., Ramirez, R., Kasting, J. F., et al. 2013, ApJ, 765, 131

Kreidberg, L., Bean, J. L., Desert, J. M., et al. 2014, Nature, 505, 69

Kreidberg, L., Koll, D. D. B., Morley, C., et al. 2019, Nature, 573, 87

Lammer, H., Erkaev, N. V., Odert, P., et al. 2013, MNRAS, 430, 1247

Lammer, H., Selsis, F., Ribas, I., et al. 2003, ApJL, 598, L121

Lammer, H., Odert, P., Leitzinger, M., et al. 2009, A&A, 506, 399

Leconte, J., Wu, H., Menou, K., & Murray, N. 2015, Science, 347, 632

Lin, S.-J., & Rood, R. B. 1996, Monthly Weather Review, 124, 2046

Lincowski, A. P., Meadows, V. S., Crisp, D., et al. 2018, ApJ, 867, 76

Lopez, E. D., & Fortney, J. J. 2014, ApJ, 792, doi:10.1088/0004-637X/792/1/1

Luger, R., & Barnes, R. 2015, Astrobiology, 15, 119

Lustig-Yaeger, J., Meadows, V. S., & Lincowski, A. P. 2019, The Astronomical Journal, 158, 27

Massie, S. T., & Hervig, M. 2013, JQSRT, 130, 373

Meixner, M., Cooray, A., Leisawitz, D., et al. 2019, arXiv e-prints, arXiv:1912.06213

Neale, R. B., Gettelman, A., Park, S., et al. 2010, in Description of the NCAR Community Atmosphere Model (CAM 5.0), Tech. Note NCAR/TN-486+STR, Natl. Cent. for Atmos, 2009–038451

Owen, J. E., & Jackson, A. P. 2012, MNRAS, 425, 2931

Quanz, S. P., Kammerer, J., Defrère, D., et al. 2018, in Society of Photo-Optical Instrumentation Engineers (SPIE) Conference Series, Vol. 10701, Proc. SPIE, 107011I

Ramirez, R. M., & Kaltenegger, L. 2014, ApJL, 797, L25

Ribas, I., Guinan, E. F., Güdel, M., & Audard, M. 2005, ApJ, 622, 680

Ricker, G. R., Winn, J. N., Vanderspek, R., et al. 2015, Journal of Astronomical Telescopes, Instruments, and Systems, 1, 014003

Roberge, A., Fischer, D., & Peterson, B. 2019, in BAAS, Vol. 51, 199

Rogers, L. A. 2015, ApJ, 801, 41

Sandu, C., Lenardic, A., & McGovern, P. 2011, Journal of Geophysical Research (Solid Earth), 116, B12404

Scalo, J., Kaltenegger, L., Segura, A. G., et al. 2007, Astrobiology, 7, 85

Schaefer, L., & Sasselov, D. 2015, ApJ, 801, 40

Schwieterman, E. W., Robinson, T. D., Meadows, V. S., Misra, A., & Domagal-Goldman, S. 2015, The Astrophysical Journal, 810, 57

Segura, A., Kasting, J. F., Meadows, V., et al. 2005, Astrobiology, 5, 706

Shields, A. L., Meadows, V. S., Bitz, C. M., et al. 2013, Astrobiology, 13, 715

Suissa, G., Mandell, A., Wolf, E. T., et al. 2019, ApJ, in review

The LUVOIR Team. 2019, arXiv e-prints, arXiv:1912.06219

Tian, F. 2009, ApJ, 703, 905

Tian, F., & Ida, S. 2015, Nature Geoscience, 8, 177

Trainer, M. G., Pavlov, Alexander, A., Curtis, D. B., et al. 2004, Astrobiology, 4, 409

Villanueva, G. L., Smith, M. D., Protopapa, S., Faggi, S., & Mandell, A. M. 2018, JQSRT, 217, 86

Watson, A. J., Donahue, T. M., & Walker, J. C. G. 1981, Icarus, 48, 150

Way, M. J., Del Genio, A. D., Kiang, N. Y., et al. 2016, Geophys. Res. Lett., 43, 8376

Way, M. J., Aleinov, I., Amundsen, D. S., et al. 2017, ApJS, 231, 12

Wolf, E. T. 2017, ApJL, 839, L1

—. 2018, ApJL), 855, L14

Wolf, E. T., Kopparapu, R. K., & Haqq-Misra, J. 2019, ApJ, 877, 35

Wolf, E. T., & Toon, O. B. 2013, Astrobiology, 13, 656

—. 2015, Journal of Geophysical Research (Atmospheres), 120, 5775

Wordsworth, R. D., Forget, F., Selsis, F., et al. 2011, ApJL, 733, L48

Wordsworth, R. D., & Pierrehumbert, R. T. 2013, ApJ, 778, 154

Yang, H. Y., Komacek, T. D., & Abbot, D. S. 2019a, ApJL, 876, L2

Yang, J., Abbot, D. S., Koll, D. D. B., Hu, Y., & Showman, A. P. 2019b, ApJ, 871, 29

Yang, J., Boué, G., Fabrycky, D. C., & Abbot, D. S. 2014, ApJL, 787, L2

Yang, J., Cowan, N. B., & Abbot, D. S. 2013, ApJL, 771, L45

Yang, J., Leconte, J., Wolf, E. T., et al. 2016, ApJ, 826, 222

Yelle, R. V. 2004, Icarus, 170, 167